Zitierweise: *Angew. Chem. Int. Ed.* **2025**, e202503100
doi.org/10.1002/anie.202503100

**Batteries**

# Stabilizing Surface Lattice $O^{n-}$ ($0 < n < 2$) for Long-Term Durability of $LiCoO_2$

*Wenguang Zhao, Mingyang Li, Zijian Li, Hengyu Ren, Xiaohu Wang, Xingxing Yin, Wangyang Ding, Guojie Chen, Shiming Chen, Haocong Yi,* Shunning Li, Jun Wang, Dong Zhou, Lin Zhou, Hai Lin, Bin Fei, Feng Pan,* and Qinghe Zhao**

**Abstract:** The instability of surface lattice $O^{n-}$ ($0 < n < 2$) in charged $LiCoO_2$ (LCO) limits its long-term cycling stability beyond 4.55 V versus $Li/Li^+$. Herein, the spinel and rock-salt (RS) phases are constructed on LCO surface to stabilize lattice $O^{n-}$, namely S-LCO and R-LCO, respectively. Upon long-term cycling at 4.6 V, the loss of lattice $O^{n-}$ leads to a progressive deterioration of surface spinel phase, which ultimately transforms into a strong $Li^+$-blocking phase. In contrast, for R-LCO, the surface lattice $O^{n-}$ in the RS phase remains stable in long-term cycles. Theoretical calculations reveal that the migration barriers of lattice $O^{n-}$ are significantly higher in the RS phase than in the spinel phase. Due to the stabilized surface lattice $O^{n-}$, the R-LCO||Li cell shows an impressive capacity retention of 78.6% after 1000 cycles at 4.6 V (at 1C rate) and superior floating charge durability at 45 °C. This study highlights the importance of surface structure tailoring in developing advanced LCO cathodes.

## Introduction

Lithium-ion batteries (LIBs) are widely used in consumer electronics, electric vehicles, and energy storage systems due to their high energy density and long cycle life.[1] $LiCoO_2$ (LCO), a successfully commercialized cathode material, offers a high theoretical capacity (274 mAh $g^{-1}$) and excellent cycle stability.[2] However, with the growing demand for LIBs, the development of high-voltage LCO is hindered by significant capacity fading caused by surface deterioration issues, which limits its further advancement and application.

The capacity fading of LCO at high voltages (>4.55 V versus $Li/Li^+$) is primarily attributed to irreversible structural phase transitions, oxidation and loss of lattice oxygen ($O^{n-}$, $0 < n < 2$), accelerated surface degradation, and detrimental side reactions on LCO surface.[3] Specifically, when the charging cutoff voltage exceeds 4.55 V, the O3 phase of LCO transforms to the H1-3 phase, and at even higher voltages, further delithiation results in the formation of the O1 phase.[4,5] These phase transitions induce Co–O layer slipping and internal lattice stress, leading to lattice distortion and potential bulk crack formation.[6–8] Additionally, during charging, the overlap of O 2p and Co 3d orbitals facilitates the electron transfer from $O^{2-}$ to $Co^{4+}$,[9] reducing the electron cloud density around O ions and promoting the redox activity of lattice $O^{n-}$.[10–12] The oxidized lattice $O^{n-}$ can accumulate and migrate to the symmetry-breaking sites in LCO structure, triggering oxygen release, which exacerbates Li/Co disorder and intensifies the irreversibility of high-voltage phase transitions.[13–15]

It is important to note that the LCO surface plays a dual role: on one hand, it serves as a necessary pathway for the migration of bulk lattice $O^{n-}$ to the surface, and on the other hand, it directly interfaces with the electrolyte, making it more prone to structural degradation.[16] The release of active lattice $O^{n-}$ at the LCO surface causes surface lattice degradation, transforming the layered structure into spinel ($Co_3O_4$) or RS (CoO) phases, which hinders the $Li^+$ transport and reduces the capacity release.[17] Furthermore, the active lattice $O^{n-}$ can react with the electrolyte, leading to electrolyte decomposition and the release of $O_2$ and $CO_2$.[18,19] These reactions result in the formation of an electrochemically unstable cathode electrolyte interphase (CEI) on LCO surface, which impedes $Li^+$ transport across

[*] W. Zhao, H. Ren, X. Wang, W. Ding, G. Chen, S. Chen, H. Yi, S. Li, L. Zhou, H. Lin, F. Pan, Q. Zhao
School of Advanced Materials, Peking University Shenzhen Graduate School Shenzhen, Shenzhen 518055, P.R. China
E-mail: yihaocong@pku.edu.cn
panfeng@pkusz.edu.cn
zhaoqh@pku.edu.cn

M. Li
Centre for Ionics University Malaya, University of Malaya, Kuala Lumpur 50603, Malaysia

Z. Li, B. Fei
School of Fashion and Textiles, The Hong Kong Polytechnic University, Kowloon, Hong Kong 999077, P.R. China

X. Yin, D. Zhou
School of Advanced Energy, Sun Yat-sen University Shenzhen Campus, Shenzhen 518107, P.R. China

J. Wang
School of Innovation and Entrepreneurship, Southern University of Science and Technology, Shenzhen 518055, P.R. China

Additional supporting information can be found online in the Supporting Information section



© 2025 Wiley-VCH GmbH

the interface, ultimately compromising the cycle stability and lifespan of LIBs.[4,20]

Among the factors contributing to the capacity fading of LCO at high voltages, the loss of lattice $O^{n-}$ is particularly prominent, especially on the LCO surface. A common approach to reduce lattice $O^{n-}$ loss is to regulate surface structure and interface chemistry.[21] Two typical approaches to surface modification involve tailoring the spinel and RS phases.[22–24] The spinel structure, belonging to the cubic crystal system of *Fd-3m*, usually tends to form a well-matched interface with the layered structure of LCO, reducing stress concentration at the interface. This minimizes the lattice $O^{n-}$ diffusion kinetics and delays the loss of lattice oxygen.[25,26] Additionally, the spinel phase provides a 3D transport channel for $Li^+$, which helps to maintain the charge balance and reduce the activity of lattice $O^{n-}$.[27,28] However, the spinel phases containing $Li^+$ are thermodynamically unstable under specific conditions and undergo structural deformation during long-term cycling, eventually transforming into an RS phase similar to the CoO structure.[29] The RS phase also belongs to the cubic crystal system *Fm-3m* but exhibits higher electrochemical stability. Its lower Co valence state alleviates catalytic effects on electrolyte decomposition, and its high thermal and structural stability resists erosion from corrosive species in the electrolyte.[30] Nevertheless, due to the lack of sufficient $Li^+$ transport channels, the RS phase exhibits lower $Li^+$ transport efficiency compared to the spinel phase.[31]

Although numerous studies have investigated surface tailoring via spinel and RS phases, there still lacks a comprehensive comparison that clarifies the differences in lattice $O^{n-}$ stability between the two phases, especially during long-term cycling. Therefore, a comprehensive analysis for both kinds of phase tailoring is essential for regulating lattice $O^{n-}$ stability in the near-surface zone of LCO and enhancing cycle stability under high-voltage conditions. In this work, the spinel and RS phases on the surface of LCO cathodes are constructed by adjusting the surface Li content. By characterizing the surface phases of cycled LCO cathodes, analyzing the correlated valence states, and performing theoretical calculations on oxygen vacancy ($O_v$) formation and migration, this work clearly illustrates the difference in the lattice $O^{n-}$ stability between the two phases. The obtained results provide critical insights into optimizing the LCO surface for improved cell performance in LIBs using LCO cathodes.

## Results and Discussion

### Regulating Surface Phase

As previously reported, the loss of lattice $O^{n-}$ in high-voltage LCO is a key factor that hinders its cycling stability. For instance, the surface of LCO undergoes a transformation from a pristine layered structure to an RS phase after 400 cycles at a current of 1 C within a voltage range of 3–4.6 V (Figure S1a,b), which is accompanied by an increase in $O_v$ on the LCO surface, as confirmed by electron energy loss spectroscopy (EELS) results (Figure S1c,d) and along with the significant generation of $O_2$, CO, and $CO_2$ (Figure S1e). To mitigate lattice $O^{n-}$ loss during long-term cycling, surface tailoring of LCO has become an essential research direction. In this work, to investigate the influence of different surface tailoring methods on the cycling stability of LCO cathodes, two kinds of LCO cathodes with surface spinel and RS phases are synthesized based on commercial LCO, named S-LCO and R-LCO, respectively. Detailed synthesis processes are provided in the Supporting Information.

As shown in Figure S2a–c, nearly the same lattice parameters are observed in S-LCO ($a = b = 2.81455$ Å, $c = 14.05187$ Å) and R-LCO ($a = b = 2.81493$ Å, $c = 14.05298$ Å) through X-ray diffraction (XRD) refinement analysis, indicating that surface tailoring does not affect bulk structure. Furthermore, according to high-angle annular dark-field scanning transmission electron microscopy (HAADF-STEM) images (Figure S2d–f), the bulk structures of regulated LCO cathodes maintain their layered structure, indicating that only the surfaces of LCO cathodes are tailored. Notably, relatively rough surfaces are observed on both the S-LCO and R-LCO surfaces (Figure S3a–c), and similar results are also confirmed by transmission electron microscopy (TEM) images (Figure S4).

Furthermore, more precise near-surface information of S-LCO and R-LCO is analyzed using HAADF-STEM. A 2 nm-thick spinel phase layer and a 2 nm-thick disordered RS phase layer are observed on the surface of S-LCO and R-LCO, respectively (Figure 1a,b). The fast Fourier transform (FFT) results further show the spinel phase on the surface of S-LCO, while the RS phase is on the surface of R-LCO. EELS analyses are further performed to investigate the distributions and local valences of Li, O, and Co in the near-surface region of LCO cathodes (Figures 1c,d and S5). According to the Li *K*-edge spectra analyses, a higher content of $Li^+$ is detected on the surface of S-LCO compared with that of R-LCO. The pre-edge of the O *K*-edge curves near 532.5 eV is associated with the transitions from O 1s to unoccupied O 2p orbitals and is regarded as indicative of the oxidation state of coordinated Co ions and $O_v$.[32] As observed, both S-LCO and R-LCO exhibit lower pre-peak intensity within approximately 3–5 nm from the surface, suggesting the presence of $O_v$ in both LCO cathodes. Since the region of $O_v$ coincides with the locations of the spinel or RS phase, the $O_v$ formation discussed in this work mainly occurs in the surface spinel or RS phases. Additionally, shifts in the Co *L*-edge peak positions in this region further indicate a reduction in the oxidation state of surface Co ions.

Figure 1e shows the O *K*-edge soft X-ray absorption spectroscopy (sXAS) in the total electron yield (TEY) mode, which is surface-sensitive (in the near-surface region of 10 nm). The results also confirm that the spinel phase (at the photon energy of 532 eV) exists on the surface of S-LCO, while the surface region of R-LCO is dominated by the RS phase (at a photon energy of 535 eV).[23,33] Raman spectra (Figure 1f) further support these conclusions, displaying two characteristic peaks located at wavenumbers 690 and 520 $cm^{-1}$, which are attributed to the presence of spinel phase on the surface of S-LCO and the RS phase on the surface of R-LCO, respectively.[34,35] Therefore, two kinds of the


© 2025 Wiley-VCH GmbH

15213757, 0, Downloaded from https://onlinelibrary.wiley.com/doi/10.1002/ange.202503100 by University Town Of Shenzhen, Wiley Online Library on [06/04/2025]. See the Terms and Conditions (https://onlinelibrary.wiley.com/terms-and-conditions) on Wiley Online Library for rules of use; OA articles are governed by the applicable Creative Commons License

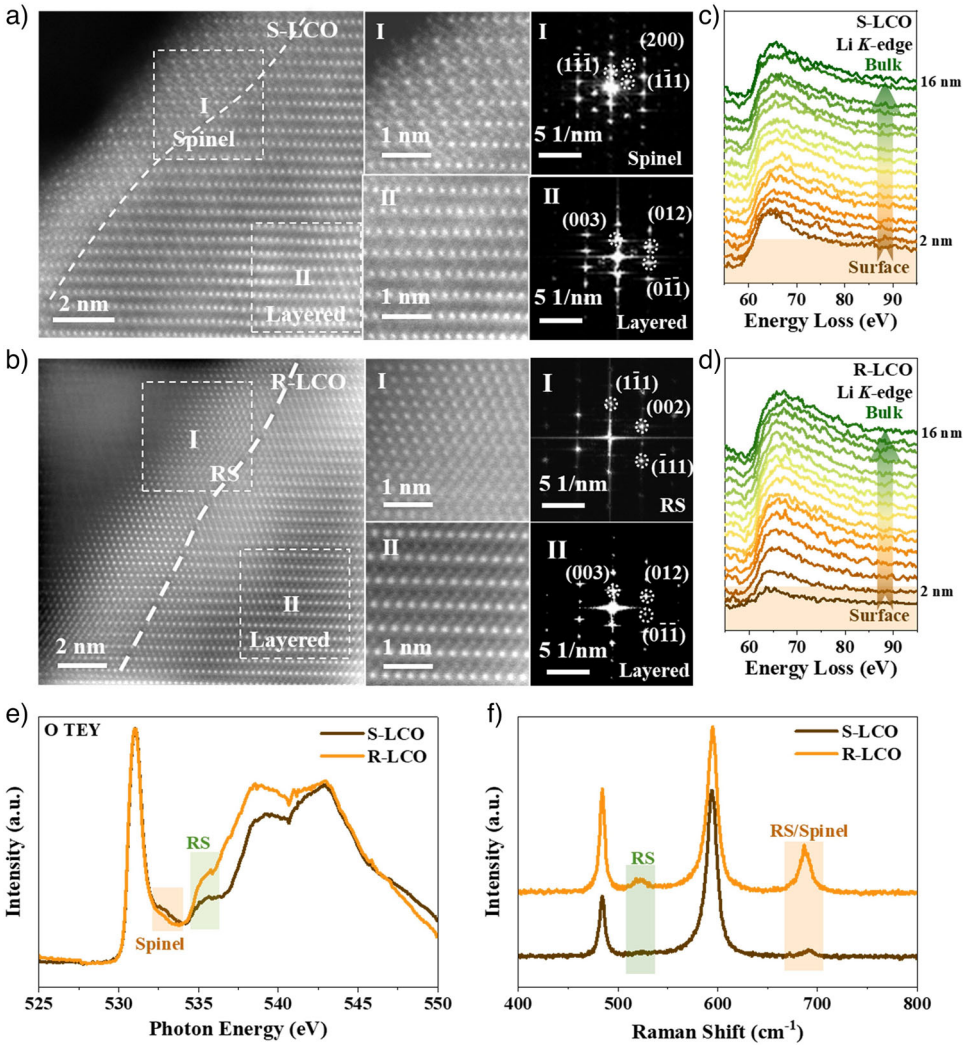


***Figure 1.*** Characterizations of two kinds of surface-tailored LCO cathodes. a) and b) HAADF-STEM images of S-LCO and R-LCO, showing the spinel and RS phase layers (~2 nm) on the surface of LCO cathodes, respectively. The inset images show corresponding area FFT patterns. c) and d) Corresponding EELS spectra curves for analyzing the $Li^+$ distribution at different etching depths. e) O *K*-edge sXAS in TEY mode of S-LCO and R-LCO, confirming the presence of spinel phase (at a photon energy of 532 eV) on the S-LCO surface and RS phase (at a photon energy of 535 eV) on the R-LCO surface. f) Raman spectra of S-LCO and R-LCO with characteristic peaks corresponding to the spinel phase on the S-LCO surface and the RS phase on the R-LCO surface.

surface-tailored LCO cathodes are successfully prepared, and their durability during long-term cycling and floating charge tests is subsequently evaluated.

### *Cycling and Floating Cell Performances*

As discussed above, the spinel and RS phases have been successfully constructed on the surface of LCO cathodes to stabilize the surface lattice $O^{n-}$. Figure S6 compares the galvanostatic charge/discharge curves of S-LCO||Li and R-LCO||Li cells in the initial three cycles. Compared with S-LCO, R-LCO presents significant polarization upon 1$^{st}$ charging, suggesting that the $Li^+$ conductivity across the RS phase is much weaker than that across the spinel phase with 3D $Li^+$ transport channels, leading to inferior rate performance. In subsequent cycles, this polarization diminishes, indicating the successful construction of the $Li^+$ migration pathway in both S-LCO and R-LCO.

To evaluate the impact of surface tailoring on the cell performance of LCO cathodes, the floating charge leakage current curves of various cells at 45 °C and 4.6 V are compared (Figure 2a). The floating charge test, which forces the highly delithiated LCO to maintain a high voltage (at 4.6 V) for an extended period, provides conditions for continuous oxidation of lattice O ions and is therefore considered an important method for evaluating side reactions between the fully charged cathode and electrolyte.[36] Compared to pristine LCO, both S-LCO and R-LCO exhibit significantly lower leakage currents (below 5 μA $mg^{-1}$) at the beginning of the floating charge and maintain lower leakage currents throughout the entire floating period (120 h). However, after approximately 5 h of floating charge, the leakage current of S-LCO shows a slight upward trend, which is attributed to


© 2025 Wiley-VCH GmbH

15213757, 0, Downloaded from https://onlinelibrary.wiley.com/doi/10.1002/ange.202503100 by University Town Of Shenzhen, Wiley Online Library on [06/04/2025]. See the Terms and Conditions (https://onlinelibrary.wiley.com/terms-and-conditions) on Wiley Online Library for rules of use; OA articles are governed by the applicable Creative Commons License

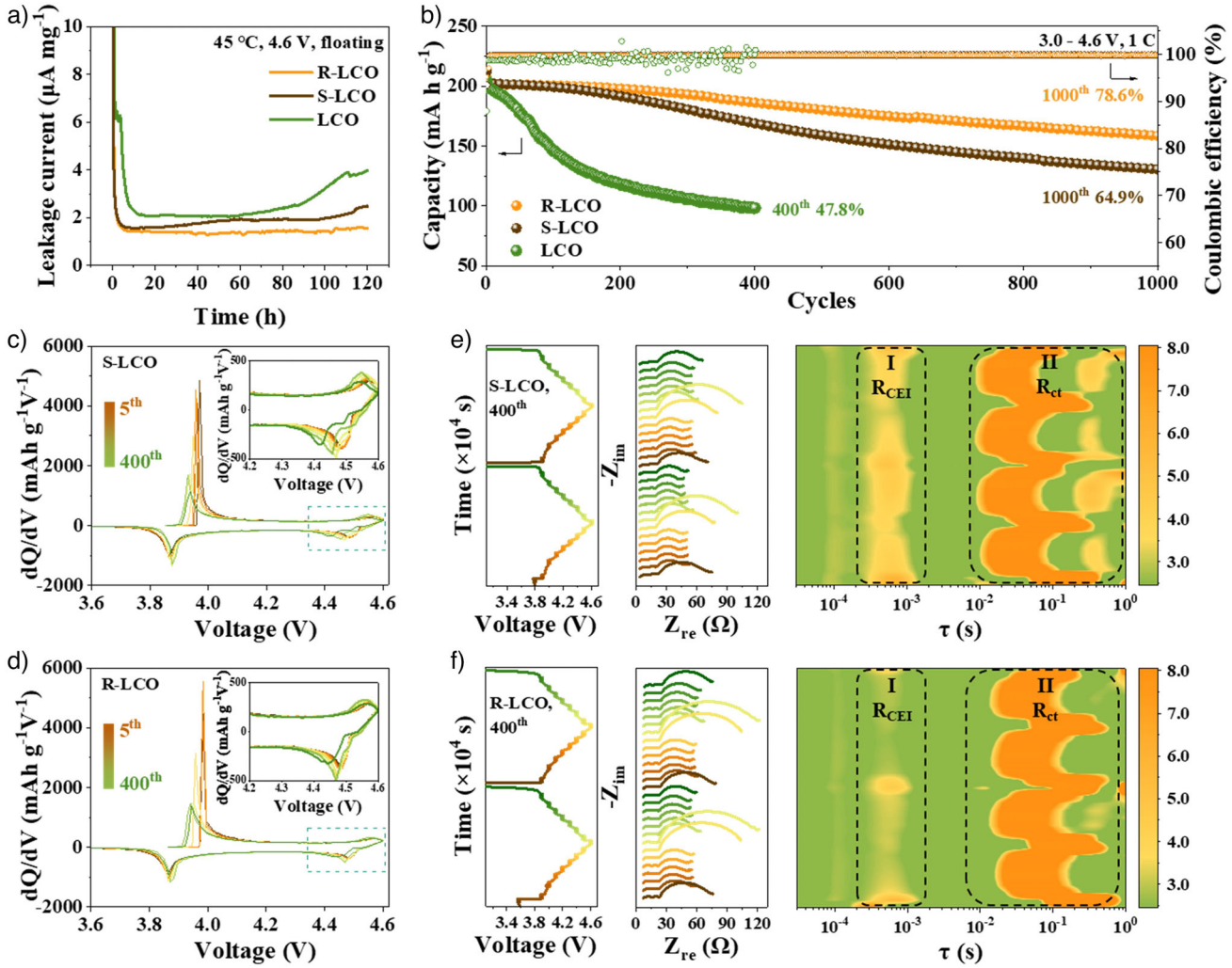


***Figure 2.*** Electrode behaviors of S-LCO||Li and R-LCO||Li cells. a) Comparison of floating charge leakage current curves of LCO||Li, S-LCO||Li, and R-LCO||Li cells at 4.6 V and 45 °C. b) Long-term cycle performances of LCO||Li, S-LCO||Li, and R-LCO||Li cells within 3–4.6 V. c and d) dQ/dV curves of S-LCO||Li and R-LCO||Li cells at the 400th cycle. e and f) In situ EIS and DRT plots of the S-LCO||Li and R-LCO||Li cells after 400 cycles. The peaks in the relaxation time range of $10^{-3}$–$10^{-4}$ s represent the transport of $Li^+$ across the CEI (section I), and the peaks in the relaxation time range of $10^{-2}$–$10^{0}$ s are related to the transport of $Li^+$ across the near-surface structure (section II).

the release of active lattice $O^{n-}$ on the surface structure of S-LCO, leading to electrolyte decomposition.

Figure 2b compares the cycle performances of the LCO||Li, S-LCO||Li, and R-LCO||Li cells within the voltage range of 3–4.6 V. Compared with pristine LCO, both S-LCO and R-LCO show significantly improved cycling stability, with discharge capacities of 130.8 and 158.7 mAh $g^{-1}$ at the 1000th cycle, corresponding to capacity retention of 64.8% and 78.6%, respectively. It is worth noting that, unlike the coulombic efficiency (CE) of LCO, which becomes disordered after about 50 cycles, the CE of both R-LCO and S-LCO remains highly stable within 1000 cycles and is very close to 100%. The cycling stability of full cells assembled with a graphite anode is also compared in Figure S7. After 200 cycles under 3–4.55 V, R-LCO and S-LCO exhibit high-capacity retention of 98.0% and 96.4%, respectively, which are significantly higher than that of the unmodified LCO (90.1%). Figures 2c,d and S8a compare the dQ/dV curves of LCO||Li, S-LCO||Li, R-LCO||Li cells during 400 cycles, and the redox peaks above 4.5 V are primarily related to the O3/H1-3 phase transition. The rapid decline of these peaks for LCO||Li cells is mainly caused by the distortion of $CoO_6$ slabs during cyclic O3/H1-3 phase transitions, accompanied by the oxidation and migration of lattice $O^{n-}$. In contrast, S-LCO and R-LCO demonstrate better stabilization of lattice $O^{n-}$, making the bulk O3/H1-3 phase transitions more reversible. Notably, R-LCO exhibits more reversible phase transitions than S-LCO, indicating that the RS phase stabilizes lattice $O^{n-}$ more effectively than the spinel phase. Consequently, the charge/discharge curves of S-LCO||Li and R-LCO||Li cells show significant differences during long-term cycling (Figure S8b–i).

To further investigate the transport characteristics of $Li^+$ in the surface-tailored S-LCO and R-LCO cathodes during long-term cycling, in situ electrochemical impedance spectroscopy (EIS) and correlated distribution of relaxation times (DRT) analyses are conducted (Figure 2e,f). The


© 2025 Wiley-VCH GmbH

15213757, 0, Downloaded from https://onlinelibrary.wiley.com/doi/10.1002/ange.202503100 by University Town Of Shenzhen, Wiley Online Library on [06/04/2025]. See the Terms and Conditions (https://onlinelibrary.wiley.com/terms-and-conditions) on Wiley Online Library for rules of use; OA articles are governed by the applicable Creative Commons License

detailed analysis procedure is illustrated in the Supporting Information. Specifically, the peaks in the relaxation time ($\tau$) range of $10^{-3}$–$10^{-4}$ s correspond to the $Li^+$ transport across the CEI, i.e., the $R_{CEI}$.[37] Compared with S-LCO, the lower intensity of $R_{CEI}$ peaks in R-LCO indicates more facilitated transport kinetics of $Li^+$ across the CEI of R-LCO. Additionally, impedance peaks in the $\tau$ range of $10^{-2}$–$10^{0}$ s are associated with $Li^+$ transport across the near-surface lattice, i.e., $R_{ct}$.[38] For S-LCO, the $\tau$ values are divided into two sections: section I (Figure 2e,f) corresponds to the $\tau$ range of $10^{-2}$–$10^{-1}$ s and section II (Figure 2e,f) refers to the $\tau$ range of $10^{-1}$–$10^{0}$ s. While for R-LCO, the $\tau$ values are mainly distributed in Section I. The results indicate that for S-LCO, the surface gradually deteriorates in 400 cycles, mainly due to the release of lattice $O^{n-}$, leading to the surface deterioration. As a result, an additional independent time constant appears in section II, correlating to more sluggish $Li^+$ transport across the deteriorated surface. For R-LCO, the surface RS phase is more stable against the release of lattice $O^{n-}$; thus, its $\tau$ values remain distributed only in section I. The in situ EIS and DRT results provide new insights into the differences between the long-term cycling stability of S-LCO and R-LCO, which are primarily attributed to the properties of the tailored surface structure and CEI. Consequently, the subsequent analyses will focus specifically on these two factors.

### *Stabilization of Surface Lattice $O^{n-}$*

To further clarify the difference in the stabilization effects of surface lattice $O^{n-}$ during long-term cycling, spherical aberration-corrected TEM images and FFT analyses of the selected areas of cycled S-LCO and R-LCO (at the 400th cycle) are further examined (Figure 3a,b). As observed, after long-term cycling, their surface structures show significant variations. For S-LCO, the surface has transformed into an RS phase with a thickness of 5 nm, which is significantly different from the pristine surface spinel phase with a thickness of 2 nm. The significant structural deterioration is mainly attributed to the formation and migration of $O_v$, which will be discussed subsequently. In contrast, R-LCO, with a structurally reinforced surface RS phase, maintains a relatively stable RS phase even after long-term cycling, with the thickness of the RS phase remaining nearly unchanged. Both the bulk structures of S-LCO and R-LCO retain their layered structure, as demonstrated by local magnification of region II, FFT results, and the fitting results obtained from the Fourier transformation based on extended X-ray absorption fine structure (EXAFS) analysis (Figure S9; Table S1).[39] The results indicate that the surface tailoring plays a dominant role in achieving better cycling durability of LCO at 4.6 V, rather than the bulk structure tailoring.

To further investigate the characteristics of lattice O ions of the cycled surface phases, EELS is performed from the surface to the bulk (Figure 3c,d). After 400 cycles, the pre-edge peaks of lattice O ions in S-LCO show reduced intensity over a range of approximately 5 nm from the surface, indicating the presence of a large amount of $O_v$.[40–42] Concurrently, the Co *L*-edge exhibits a significant shift in peak position within 5 nm from the surface (Figure S10), indicating a reduction in the oxidation state of surface Co ions. After 400 cycles, the original spinel surface of S-LCO cannot be maintained due to the large-scale formation and migration of $O_v$, and lattice O ions passively participate in the charge transfer process upon charging, leading to the deterioration of the spinel phase into an RS phase similar to the structure of CoO with a large number of $O_v$. In contrast, for R-LCO, attributed to the tailored surface RS phase, a stable RS phase of about 2 nm thick is retained even after 400 cycles at 4.6 V.

Furthermore, the pre-edge peaks of the O *K*-edge in sXAS provide additional structural information relating to the chemical bonds between O and Co ions (Figure 3e). The position of the pre-edge peaks is related to the electronic structure of O ions and their bonding characteristics with the Co ions. The peak located at 530.9 eV in the O *K*-edge spectrum, observed before cycling, is associated with the transition of electrons from O 1s to the hole state of the O 2p energy level.[43] For the cycled S-LCO and R-LCO cathodes, a new peak located at 532.6 eV appears, which refers to the signal of the RS phase.[44] As observed, the higher intensity of this new peak in cycled S-LCO indicates a thicker RS phase in S-LCO than that in R-LCO. Additionally, the peak located at 533.8 eV for cycled S-LCO suggests an increased content of $Li_2CO_3$ on the surface, implying a greater degree of side reactions.[45] In the Co *L*-edge spectrum, the $L_3$ and $L_2$ peaks are related to the transition of Co $2p_{3/2}$ and Co $2p_{1/2}$ electrons to unoccupied 3d levels that are highly hybridized with O 2p orbitals (Figure 3f).[43] The new peaks appearing at 778.3, 779.7, 780.1, and 795.3 eV in cycled S-LCO are related to the formation of low-valence Co,[46] indicating more severe phase changes in S-LCO. The sXAS measurements of O *K*-edge spectrum of the floated S-LCO and R-LCO (after 120 h of floating) indicate that R-LCO shows more peaks corresponding to $Co^{4+}$ (Figure 3g), suggesting that it can maintain the highly delithiated O1 phase, namely $CoO_2$, without structural collapse or changes in valence.[47,48] The higher $L_2/L_3$ ratio in the Co *L*-edge spectrum also confirms that the Co valence in the floated R-LCO is higher (Figure 3h). In contrast, for S-LCO, the structure collapse is due to its inability to maintain the O1 phase, which is the root cause of cracks.

### *Optimized Cathode/Electrolyte Interphase*

Besides variations in surface structure tailoring, the difference between long-term cycle performances of S-LCO and R-LCO is also attributed to the stability of their CEI layers. After 400 cycles, the composition and morphology of the surface CEI for S-LCO and R-LCO exhibit significant differences. Figure 4a,b compares the F 1s spectra of S-LCO and R-LCO after 400 cycles, where peaks located at binding energies of 688, 686.6, and 685 eV correspond to -$CF_2$, $Li_xPF_yO_z$, and LiF species, respectively.[49] The presence of more $Li_xPF_yO_z$ species in cycled S-LCO indicates that electrolyte decomposition is more severe due to the oxidized lattice $O^{n-}$ on the surface. In contrast, R-LCO exhibits a higher content of LiF, and its inorganic component-dominated CEI suggests


© 2025 Wiley-VCH GmbH

15213757, 0, Downloaded from https://onlinelibrary.wiley.com/doi/10.1002/ange.202503100 by University Town Of Shenzhen, Wiley Online Library on [06/04/2025]. See the Terms and Conditions (https://onlinelibrary.wiley.com/terms-and-conditions) on Wiley Online Library for rules of use; OA articles are governed by the applicable Creative Commons License

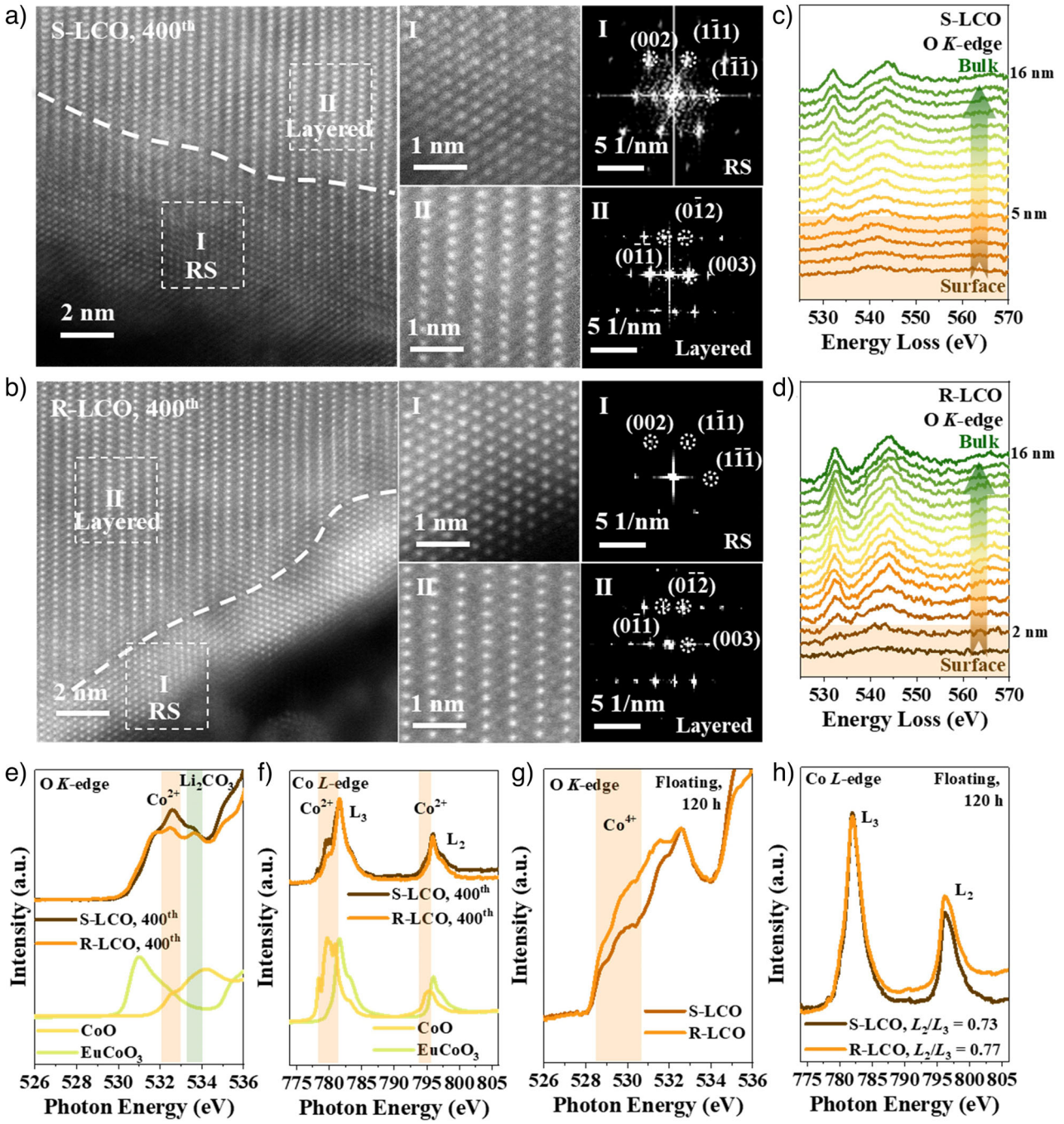


***Figure 3.*** Stabilizing effects of surface-tailored phases. a and b) HAADF-STEM images and selected area FFT patterns of cycled S-LCO and R-LCO after 400 cycles. c and d) EELS analysis from surface to bulk direction, showing the degree of $O_v$ formation. e and f) O *K*-edge and Co *L*-edge of sXAS spectra for S-LCO and R-LCO before and after cycling. g and h) O *K*-edge and Co *L*-edge of sXAS spectra for S-LCO and R-LCO before and after floating.

greater toughness. Figure 4c,d compares the O 1s spectra of S-LCO and R-LCO cathodes after 400 cycles, where peaks located at binding energies of 534.6, 533.5, 532, and 529.8 eV correspond to $Li_xPF_yO_z$, C—O, C═O, and lattice O species, respectively.[50] For cycled R-LCO, more pronounced lattice O and fewer peaks associating with the organic decomposition products are observed on the surface, indicating fewer side reactions on the surface of R-LCO.

The different side reactions on the surface of S-LCO and R-LCO lead to significant differences in CEI morphologies. Cryo-TEM is used to compare the CEI morphology of S-LCO and R-LCO cathodes after 400 cycles (Figure 4e,f). Compared with the cycled S-LCO, which has a thicker and uneven CEI, the CEI of cycled R-LCO displays a thin and uniform morphology, as observed by scanning electron microscope (SEM) (Figure S11). Thus, the RS phase, due to


© 2025 Wiley-VCH GmbH

15213757, 0, Downloaded from https://onlinelibrary.wiley.com/doi/10.1002/ange.202503100 by University Town Of Shenzhen, Wiley Online Library on [06/04/2025]. See the Terms and Conditions (https://onlinelibrary.wiley.com/terms-and-conditions) on Wiley Online Library for rules of use; OA articles are governed by the applicable Creative Commons License

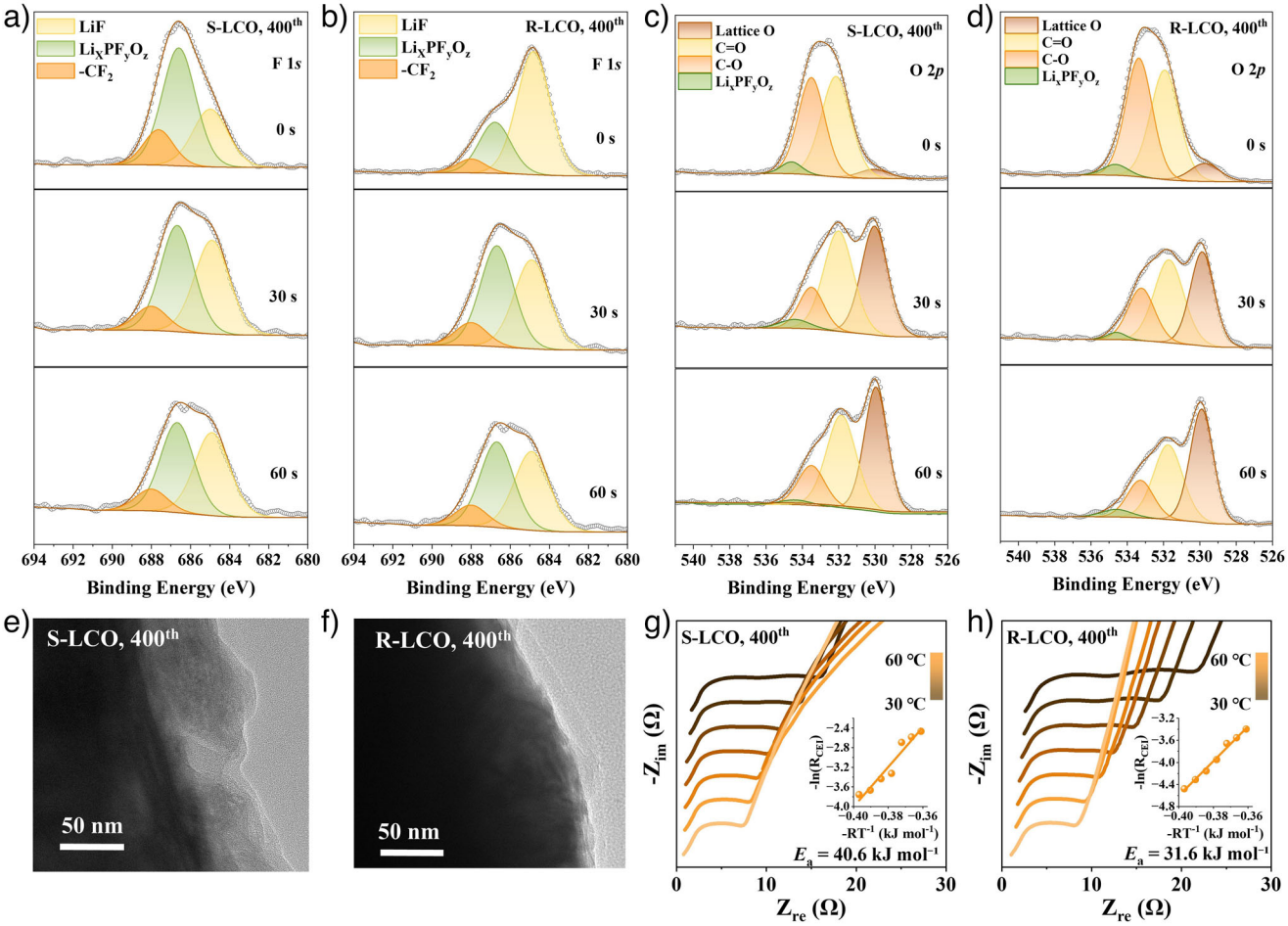


***Figure 4.*** Characterization of the CEI layers on cycled S-LCO and R-LCO cathodes. a and b) F 1s spectra of S-LCO and R-LCO after 400 cycles, where the peaks located at binding energies of 688, 686.6, and 685 eV correspond to —$CF_2$, $Li_xPF_yO_z$, and LiF species, respectively. c and d) O 1s spectra of S-LCO and R-LCO after 400 cycles, where the peaks located at binding energies of 534.6, 533.5, 532, and 529.8 eV correspond to $Li_xPF_yO_z$, C—O, C═O, and lattice O species, respectively. e and f) Cryo-TEM images showing the CEI morphology of S-LCO and R-LCO after 400 cycles. g and h) The temperature-dependent impedance measurements from 30 to 60 °C and the corresponding activation energy calculations for S-LCO and R-LCO after 400 cycles.

its stabilizing effect on lattice $O^{n-}$, can significantly optimize the composition and morphology of the CEI on the surface of R-LCO during cycling, which directly enhances the $Li^+$ diffusion kinetics of CEI. To explore the $Li^+$ diffusion barriers in various CEI layers, temperature-dependent impedance measurements are performed as the operating temperature increases from 30 to 60 °C (Figure 4g,h). Activation energy calculations reveal that the diffusion barrier of $Li^+$ ions in the CEI of S-LCO ($E_a = 40.6$ kJ mol$^{-1}$) is significantly higher than that in the CEI of R-LCO ($E_a = 31.6$ kJ mol$^{-1}$). This implies that the thin and uniform CEI, dominated by the inorganic components and formed on cycled R-LCO, is more favorable for the efficient $Li^+$ transport.

Electrolyte decomposition induced by the O release at 4.6 V is revealed via the DEMS and in situ infrared (IR) spectroscopy in the 1st cycle (Figure S12). At high voltages, a small amount of oxygen escapes from the surface of S-LCO, reacting with the electrolyte to form $CO_2$ gas. The in situ IR spectroscopy further confirms the occurrence of interfacial side reactions in both surface-tailored LCO cathodes. Compared with R-LCO, S-LCO exhibits a characteristic absorption peak around 2349 cm$^{-1}$, corresponding to $CO_2$ produced by electrolyte decomposition. Additionally, the peaks associated with the solvent decomposition product RCOO-Li in the wavenumbers of 1400–1600 cm$^{-1}$ are more pronounced in S-LCO.[51–53] Furthermore, it is reported that floating charge, an important test procedure for measuring the extent of side reactions, can clearly reflect the side reactions on the surface of LCO cathodes. After 120 h of floating charge at 4.6 V, S-LCO not only develops obvious cracks but also forms a non-uniform and thicker CEI layer on its surface (Figure S13). In contrast, R-LCO shows much fewer cracks, and its CEI remains thin and uniform.

### *Theoretical Calculation of $O_v$ Migration*

As clarified above, the long-term cycling stability of LCO cathodes varies significantly due to the different stability of lattice $O^{n-}$ in spinel and RS phases. To further investigate


© 2025 Wiley-VCH GmbH

15213757, 0, Downloaded from https://onlinelibrary.wiley.com/doi/10.1002/ange.202503100 by University Town Of Shenzhen, Wiley Online Library on [06/04/2025]. See the Terms and Conditions (https://onlinelibrary.wiley.com/terms-and-conditions) on Wiley Online Library for rules of use; OA articles are governed by the applicable Creative Commons License

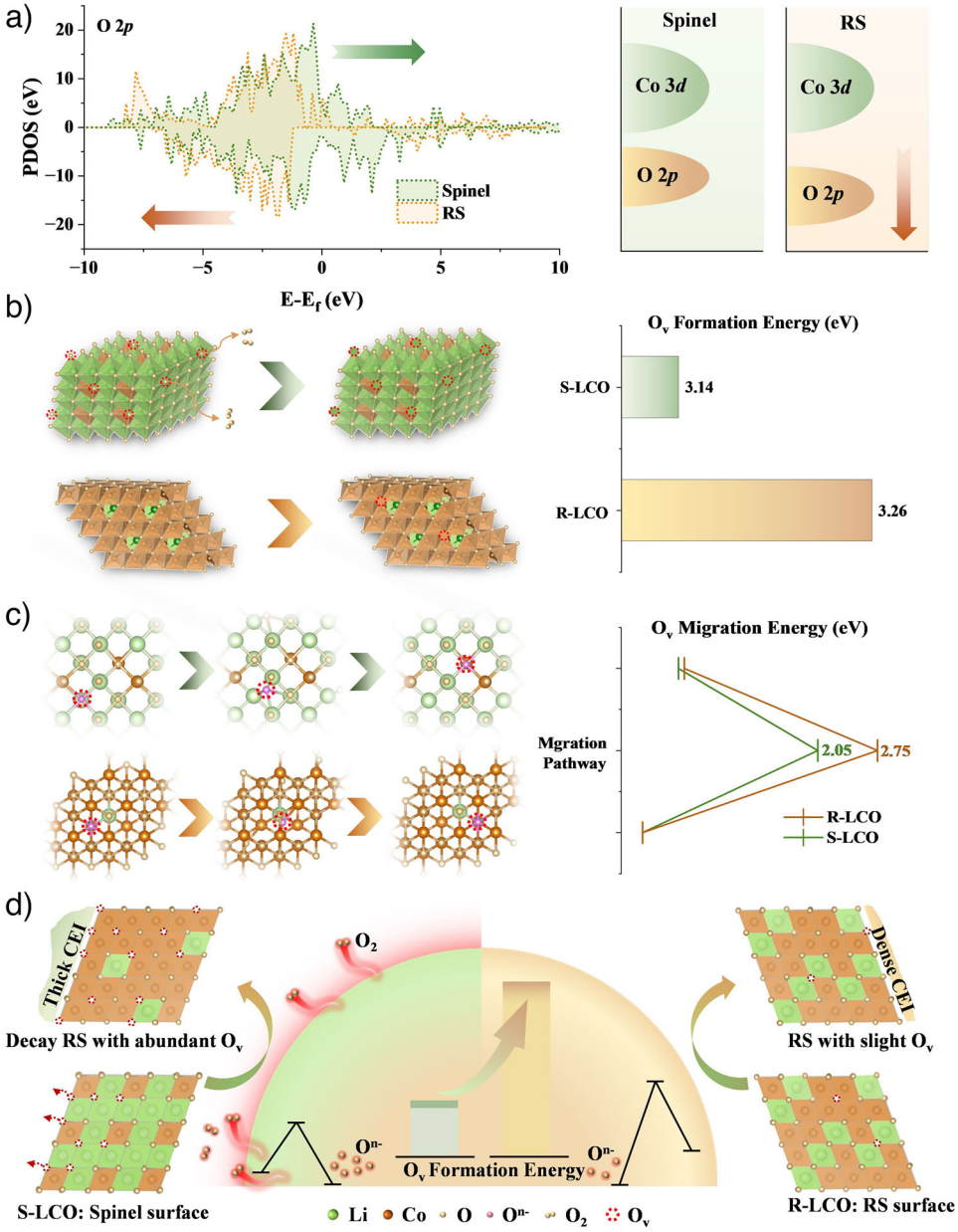


***Figure 5.*** Theoretical calculations of $O_v$ formation and migration in spinel and RS structures. a) Comparison of PDOS results for the spinel phase of S-LCO and the RS phase of R-LCO. b) DFT calculations of the formation energy of $O_v$ in the spinel phase on the S-LCO surface and the RS phase on the R-LCO surface. Based on DFT calculation results, $O_v$ is more likely to form in the spinel phase of S-LCO, while lattice O ions in the RS phase of R-LCO are more stable. c) Comparison of the $O_v$ migration energy barriers, revealing that the RS phase significantly suppresses short-range diffusion of Ov. d) Schematic illustration of the evolution of lattice O in the surface spinel phase of S-LCO and the RS phase of R-LCO during long-term cycling.

the distinct roles of these surface phases in stabilizing lattice $O^{n-}$, partial density of states (PDOS) calculations for S-LCO and R-LCO were compared. The band centers of O 2p orbitals in delithiated spinel phase of S-LCO and RS phase of R-LCO are −1.34 and −2.32 eV, respectively (Figure 5a). This means that the O 2p band center of RS phase presents relatively lower Fermi level, implying that it is more difficult for electrons transferring from O 2p to Co 3d.[54] As a result, R-LCO exhibits lower oxygen redox activity. Notably, the redox-active lattice $O^{n-}$ can migrate via $O_v$ during charging and can be released in the form of $O_2$, causing irreversible structural degradation. Moreover, as O loss occurs, the intensity of $O_v$ increases, further promoting the lattice $O^{n-}$ migration. Thus, studying the formation and migration of $O_v$ is crucial for understanding the mechanism by which the spinel and RS phases stabilize surface lattice $O^{n-}$. Density functional theory (DFT) calculations further reveal the formation energy of $O_v$ in spinel and RS phases (Figure 5b). For the spinel phase in S-LCO, under high delithiation states, the oxidation of lattice oxygen can be initiated and lead to the formation of oxidized lattice $O^{n-}$ and even $O_2$.[4,55] That is to say, the covalency between Co


© 2025 Wiley-VCH GmbH

15213757, 0, Downloaded from https://onlinelibrary.wiley.com/doi/10.1002/ange.202503100 by University Town Of Shenzhen, Wiley Online Library on [06/04/2025]. See the Terms and Conditions (https://onlinelibrary.wiley.com/terms-and-conditions) on Wiley Online Library for rules of use; OA articles are governed by the applicable Creative Commons License

and O ions of spinel phase becomes relatively weaker, making the lattice Co ions more prone to migrate[56,57] and ultimately deteriorated to form a thick RS phase after 400 cycles.

In contrast, the strong Co-O covalency in the RS phase of R-LCO significantly restrains the formation and migration of $O_v$. The enhanced bonding between Co and O ions in the RS phase at highly charged states plays a critical role in stabilizing lattice $O^{n-}$. DFT calculations confirm that $O_v$ formation is more likely in the spinel phase of S-LCO, while lattice $O^{n-}$ in the RS phase of R-LCO remains more stable. Additionally, the migration of $O_v$ differs significantly between the two phases. In the RS phase, the migration of $O_v$ is suppressed, whereas in the spinel phase, $O_v$ readily forms and migrates, causing local lattice disorder and leading to the formation of an RS phase with an Wabundant amount of $O_v$ (Figure 5c).[58]

This work highlights the application of surface spinel and RS phases to reduce LCO surface degradation during long-term cycling, as illustrated in Figure 5d. By regulating the surface phases, the cycling stability of LCO cathodes is significantly enhanced via stabilizing the surface lattice $O^{n-}$. Differences in the formation and migration of $O_v$ between the two phases lead to variations in cycling stability, phase structure, and CEI layer evolution. The surface spinel phase, due to its relatively lower ability to stabilize lattice $O^{n-}$, experiences greater structural degradation and forms an uneven CEI. In contrast, the strongly covalent RS phase demonstrates a superior stabilizing effect on lattice $O^{n-}$, maintaining a stable phase structure and a uniform CEI layer during long-term cycling.

In this work, the key role of surface structure regulation in stabilizing the surface lattice $O^{n-}$ is emphasized, and the strongly covalent RS phase is proposed as a reinforcing surface structure, where $O_v$ is difficult to form and migrate, effectively suppressing the loss of lattice $O^{n-}$ and the occurrence of side reactions, thereby achieving a high-capacity retention of 78.6% in 1000 cycles at 4.6 V. The strategy of utilizing the RS phase to stabilize surface lattice $O^{n-}$ at high voltages can also be applied to other layered oxide cathodes. In the future, we suggest that researchers conduct more comprehensive investigations on the synthesis of surface RS phase to make it more cost-effective, enhance its performance, and promote mass production. The obtained results will benefit the development of more advanced batteries based on LCO cathodes.

## Conclusion

In summary, this work investigates the feasibility and mechanism of utilizing surface spinel and RS phases to stabilize surface lattice $O^{n-}$ in the charged LCO cathodes for enhanced long-term cycling stability beyond 4.55 V. The spinel and RS phases are successfully constructed on the surface of S-LCO and R-LCO by adjusting the surface $Li^+$ content, respectively. The formation and migration of $O_v$ in these surface phases are found to dominate their long-term cycling stability, as well as the evolution of the cycled surface structure and CEI. The surface spinel phase in S-LCO gradually degrades due to the release of surface lattice $O^{n-}$ upon long-term cycles at 4.6 V, leading to the formation of a thick RS phase, which acts as a strong $Li^+$ blocking layer. In contrast, the surface RS phase in R-LCO remains stable during long-term cycling, effectively suppressing side reactions and achieving a high-capacity retention of 78.6% in 1000 cycles at 4.6 V. Overall, this work underscores the critical role of surface structure tailoring in stabilizing the surface lattice $O^{n-}$, providing new insights for the design and development of high-voltage and long-lifespan LCO cathodes.

## Supporting Information

The experimental procedures and the supporting data are presented in the Supporting Information.

## Acknowledgements

This work was financially supported by the National Natural Science Foundation of China (Grant No. 92472206), the Major Science and Technology Infrastructure Project of Material Genome Big-Science Facilities Platform supported by the Municipal Development and Reform Commission of Shenzhen, the International Joint Research Center for Electric Vehicle Power Battery and Materials (No. 2015B01015), the Guangdong Key Laboratory of Design and Calculation of New Energy Materials (No. 2017B030301013), and the Shenzhen Key Laboratory of New Energy Resources Genome Preparation and Testing (No. ZDSYS201707281026184). The authors also acknowledge the Helmholtz-Zentrum Berlin für Materialien und Energie for the allocation of synchrotron radiation beamtime at the GELEM Dipole. The GELEM-PES Endstation at HZB received funding from the BMBF program ErUM-Pro.

## Conflict of Interests

The authors declare no conflict of interest.

## Data Availability Statement

The data that support the findings of this study are available from the corresponding author upon reasonable request.

**Keywords:** $LiCoO_2$ · Li-ion batteries · Rock-salt · Spinel · Surface tailoring

[1] M. Yoon, Y. Dong, J. Hwang, J. Sung, H. Cha, K. Ahn, Y. Huang, S. J. Kang, J. Li, J. Cho, *Nat. Energy* **2021**, *6*, 362–371.
[2] C. Lin, J. Li, Z.-W. Yin, W. Huang, Q. Zhao, Q. Weng, Q. Liu, J. Sun, G. Chen, F. Pan, *Adv. Mater.* **2024**, *36*, 2307404.


© 2025 Wiley-VCH GmbH

15213757, 0, Downloaded from https://onlinelibrary.wiley.com/doi/10.1002/ange.202503100 by University Town Of Shenzhen, Wiley Online Library on [06/04/2025]. See the Terms and Conditions (https://onlinelibrary.wiley.com/terms-and-conditions) on Wiley Online Library for rules of use; OA articles are governed by the applicable Creative Commons License

[3] H. Yi, Y. Du, J. Fang, Z. Li, H. Ren, W. Zhao, H. Chen, L. Zhou, Q. Zhao, F. Pan, *ACS Appl. Mater. Interfaces* **2023**, *15*, 42667–42675.

[4] Z. Wu, G. Zeng, J. Yin, C.-L. Chiang, Q. Zhang, B. Zhang, J. Chen, Y. Yan, Y. Tang, H. Zhang, S. Zhou, Q. Wang, X. Kuai, Y.-G. Lin, L. Gu, Y. Qiao, S.-G. Sun, *ACS Energy Lett.* **2023**, *8*, 4806–4817.

[5] Y. Huang, Y. Zhu, H. Fu, M. Ou, C. Hu, S. Yu, Z. Hu, C.-T. Chen, G. Jiang, H. Gu, H. Lin, W. Luo, Y. Huang, *Angew. Chem. Int. Ed.* **2021**, *60*, 4682–4688.

[6] W. Huang, J. Li, Q. Zhao, S. Li, M. Ge, J. Fang, Z. Chen, L. Yu, X. Huang, W. Zhao, X. Huang, G. Ren, N. Zhang, L. He, J. Wen, W. Yang, M. Zhang, T. Liu, K. Amine, F. Pan, *Adv. Mater.* **2024**, *36*, 2405519.

[7] H. Ren, W. Zhao, H. Yi, Z. Chen, H. Ji, Q. Jun, W. Ding, Z. Li, M. Shang, J. Fang, K. Li, M. Zhang, S. Li, Q. Zhao, F. Pan, *Adv. Funct. Mater.* **2023**, *33*, 2302622.

[8] Z. Li, H. Yi, W. Ding, H. Ren, Y. Du, M. Shang, W. Zhao, H. Chen, L. Zhou, H. Lin, Q. Zhao, F. Pan, *Adv. Funct. Mater.* **2024**, *34*, 2312837.

[9] N. Qin, Q. Gan, Z. Zhuang, Y. Wang, Y. Li, Z. Li, I. Hussain, C. Zeng, G. Liu, Y. Bai, K. Zhang, Z. Lu, *Adv. Energy Mater.* **2022**, *12*, 2201549.

[10] Q. Zhao, F. Pan, *Joule* **2024**, *8*, 2187–2189.

[11] W. Kong, J. Zhang, D. Wong, W. Yang, J. Yang, C. Schulz, X. Liu, *Angew. Chem. Int. Ed.* **2021**, *60*, 27102–27112.

[12] E. Hu, Q. Li, X. Wang, F. Meng, J. Liu, J.-N. Zhang, K. Page, W. Xu, L. Gu, R. Xiao, H. Li, X. Huang, L. Chen, W. Yang, X. Yu, X.-Q. Yang, *Joule* **2021**, *5*, 720–736.

[13] Z. Chen, W. Zhang, J. Liu, M. Zhang, S. Li, F. Pan, *Adv. Mater.* **2024**, *36*, 2403307.

[14] A. Gao, L. Gu, *Adv. Funct. Mater.* **2025**, *35*, 2409372.

[15] Q. Wang, Z. Yao, J. Wang, H. Guo, C. Li, D. Zhou, X. Bai, H. Li, B. Li, M. Wagemaker, C. Zhao, *Nature* **2024**, *629*, 341–347.

[16] S. Sharifi-Asl, J. Lu, K. Amine, R. Shahbazian-Yassar, *Adv. Energy Mater.* **2019**, *9*, 1900551.

[17] R. Konar, S. Maiti, N. Shpigel, D. Aurbach, *Energy Storage Mater.* **2023**, *63*, 103001.

[18] Z. Zhu, D. Yu, Z. Shi, R. Gao, X. Xiao, I. Waluyo, M. Ge, Y. Dong, W. Xue, G. Xu, W.-K. Lee, A. Hunt, J. Li, *Energy Environ. Sci.* **2020**, *13*, 1865–1878.

[19] H. Ren, G. Zheng, Y. Li, S. Chen, X. Wang, M. Zhang, W. Zhao, H. Yi, W. Huang, J. Fang, T. Liu, L. Yang, M. Liu, Q. Zhao, F. Pan, *Energy Environ. Sci.* **2024**, *17*, 7944–7957.

[20] J.-J. Fang, Y.-H. Du, Z.-J. Li, W.-G. Fan, H.-Y. Ren, H.-C. Yi, Q.-H. Zhao, F. Pan, *J. Electrochem.* **2024**, *30*, 2314005.

[21] H. Ren, J. Hu, H. Ji, Y. Huang, W. Zhao, W. Huang, X. Wang, H. Yi, Y. Song, J. Liu, T. Liu, M. Liu, Q. Zhao, F. Pan, *Adv. Mater.* **2024**, *36*, 2408875.

[22] X. Wang, H. Ren, Y. Du, Z. Li, W. Zhao, H. Ji, H. Yi, Q. Pan, J. Liu, Z. Lou, L. Zhou, F. Pan, Q. Zhao, *Nano Energy* **2024**, *125*, 109537.

[23] W. Ding, H. Ren, Z. Li, M. Shang, Y. Song, W. Zhao, L. Chang, T. Pang, S. Xu, H. Yi, L. Zhou, H. Lin, Q. Zhao, F. Pan, *Adv. Energy Mater.* **2024**, *14*, 2303926.

[24] J. Liu, J. Wang, Y. Ni, J. Liu, Y. Zhang, Y. Lu, Z. Yan, K. Zhang, Q. Zhao, F. Cheng, J. Chen, *Angew. Chem. Int. Ed.* **2022**, *61*, e202207000.

[25] C. Zhang, X. Shen, X. Li, Q. Liu, Z. Liu, Y. Huang, Y. Gao, Z. Hu, J.-M. Chen, Y. Yang, J. Ma, S.-C. Haw, X. Wang, R. Yu, Z. Wang, L. Chen, *Chem. Mater.* **2023**, *35*, 6692–6701.

[26] Z. Zhuang, J. Wang, K. Jia, G. Ji, J. Ma, Z. Han, Z. Piao, R. Gao, H. Ji, X. Zhong, G. Zhou, H.-M. Cheng, *Adv. Mater.* **2023**, *35*, 2212059.

[27] J. Lu, Y.-L. Chang, B. Song, H. Xia, J.-R. Yang, K. S. Lee, L. Lu, *J. Power Sources* **2014**, *271*, 604–613.

[28] H. Ma, F. Wang, M. Shen, Y. Tong, H. Wang, H. Hu, *Small Methods* **2024**, *8*, 2300820.

[29] M. J. Ramirez-Peral, J. Diaz-Sanchez, A. Galindo, M. L. Crespillo, H. P. van der Meulen, C. Morant, C. Polop, E. Vasco, *Energy Storage Mater.* **2024**, *71*, 103658.

[30] S. Qi, Y. Guan, J. Wang, R. Xia, L. Zhang, J. Li, C. Sun, Q. An, K. Zhao, *Energy Environ. Sci.* **2024**, *17*, 2269–2278.

[31] Z. Bi, Z. Yi, L. Zhang, G. Wang, A. Zhang, S. Liao, Q. Zhao, Z. Peng, L. Song, Y. Wang, Z. Zhao, S. Wei, W. Zhao, X. Shi, M. Li, N. Ta, J. Mi, S. Li, P. Das, Y. Cui, C. Chen, F. Pan, Z.-S. Wu, *Energy Environ. Sci.* **2024**, *17*, 2765–2775.

[32] S. Ostanin, A. J. Craven, D. W. McComb, D. Vlachos, A. Alavi, M. W. Finnis, A. T. Paxton, *Phys. Rev. B* **2000**, *62*, 14728–14735.

[33] Y. Yan, Q. Fang, X. Kuai, S. Zhou, J. Chen, H. Zhang, X. Wu, G. Zeng, Z. Wu, B. Zhang, Y. Tang, Q. Zheng, H.-G. Liao, K. Dong, I. Manke, X. Wang, Y. Qiao, S.-G. Sun, *Adv. Mater.* **2024**, *36*, 2308656.

[34] A. Sivakumar, S. Soundarya, S. S. Jude Dhas, K. K. Bharathi, S. A. M. B. Dhas, *J. Phys. Chem. C* **2020**, *124*, 10755–10763.

[35] S. J. Bae, K. Uk, O. Dymshits, A. Shashkin, M. Tsenter, A. Zhilin, *J. Non-Cryst. Solids* **2005**, *351*, 2969–2978.

[36] M. Hirooka, T. Sekiya, Y. Omomo, M. Yamada, H. Katayama, T. Okumura, Y. Yamada, K. Ariyoshi, *Electrochim. Acta* **2019**, *320*, 134596.

[37] Y. Lu, C. Z. Zhao, J. Q. Huang, Q. Zhang, *Joule* **2022**, *6*, 1172–1198.

[38] R. Qin, S. Ding, C. Hou, L. Liu, Y. Wang, W. Zhao, L. Yao, Y. Shao, R. Zou, Q. Zhao, S. Li, F. Pan, *Adv. Energy Mater.* **2023**, *13*, 2203915.

[39] C. Ekwongsa, S. Rujirawat, P. Butnoi, N. Vittayakorn, M. Suttapun, R. Yimnirun, P. Kidkhunthod, *Radiat. Phys. Chem.* **2020**, *175*, 108545.

[40] F. Lin, D. Nordlund, I. M. Markus, T.-C. Weng, H. L. Xin, M. M. Doeff, *Energy Environ. Sci.* **2014**, *7*, 3077.

[41] F. Lin, I. M. Markus, D. Nordlund, T.-C. Weng, M. D. Asta, H. L. Xin, M. M. Doeff, *Nat. Commun.* **2014**, *5*, 3529.

[42] S. Li, K. Li, J. Zheng, Q. Zhang, B. Wei, X. Lu, *J. Phys. Chem. Lett.* **2019**, *10*, 7537–7546.

[43] W.-S. Yoon, K.-B. Kim, M.-G. Kim, M.-K. Lee, H.-J. Shin, J.-M. Lee, J.-S. Lee, C.-H. Yo, *J. Phys. Chem. B.* **2002**, *106*, 2526–2532.

[44] S. Tan, Z. Shadike, J. Li, X. Wang, Y. Yang, R. Lin, A. Cresce, J. Hu, A. Hunt, I. Waluyo, L. Ma, F. Monaco, P. Cloetens, J. Xiao, Y. Liu, X.-Q. Yang, K. Xu, E. Hu, *Nat. Energy* **2022**, *7*, 484–494.

[45] H. Zhuo, Y. Liu, Z. Wang, A. Zhang, Z. Li, Z. Ren, X. Liu, H. Peng, L. Wang, J. Shi, X. Sun, S. Lu, D. Xia, W. Zhuang, *Nano Energy* **2021**, *83*, 105812.

[46] D. Leanza, C. A. F. Vaz, G. Melinte, X. Mu, P. Novák, M. El Kazzi, *ACS Appl. Mater. Interfaces* **2019**, *11*, 6054–6065.

[47] S. Li, Y. Sun, A. Gao, Q. Zhang, X. Lu, X. Lu, *Proc. Natl. Acad. Sci.* **2022**, *119*, e2120060119.

[48] Y.-S. Hong, X. Huang, C. Wei, J. Wang, J.-N. Zhang, H. Yan, Y. S. Chu, P. Pianetta, R. Xiao, X. Yu, Y. Liu, H. Li, *Chem* **2020**, *6*, 2759–2769.

[49] Z. Li, H. Yi, H. Ren, J. Fang, Y. Du, W. Zhao, H. Chen, Q. Zhao, F. Pan, *Adv. Funct. Mater.* **2023**, *33*, 2307913.

[50] Y.-C. Lu, A. N. Mansour, N. Yabuuchi, Y. Shao-Horn, *Chem. Mater.* **2009**, *21*, 4408–4424.

[51] Y. Wang, Y. Zhao, S. Zhang, L. Shang, Y. Ni, Y. Lu, Y. Li, Z. Yan, Z. Miao, J. Chen, *Angew. Chem. Int. Ed.* **2024**, *63*, e202412108.

[52] Z. Li, W. Zhao, H. Ren, H. Yi, Y. Du, H. Yu, J. Fang, Y. Song, H. Chen, L. Zhou, S. Li, Q. Zhao, F. Pan, *Adv. Energy Mater.* **2024**, *14*, 2402223.




© 2025 Wiley-VCH GmbH

15213757, 0, Downloaded from https://onlinelibrary.wiley.com/doi/10.1002/ange.202503100 by University Town Of Shenzhen, Wiley Online Library on [06/04/2025]. See the Terms and Conditions (https://onlinelibrary.wiley.com/terms-and-conditions) on Wiley Online Library for rules of use; OA articles are governed by the applicable Creative Commons License

[53] W. Dong, B. Ye, M. Cai, Y. Bai, M. Xie, X. Sun, Z. Lv, F. Huang, *ACS Energy Lett.* **2023**, *8*, 881–888.
[54] M. Cai, Y. Dong, M. Xie, W. Dong, C. Dong, P. Dai, H. Zhang, X. Wang, X. Sun, S. Zhang, M. Yoon, H. Xu, Y. Ge, J. Li, F. Huang, *Nat. Energy* **2023**, *8*, 159–168.
[55] H. Chen, M. S. Islam, *Chem. Mater.* **2016**, *28*, 6656–6663.
[56] G. Ceder, Y. M. Chiang, D. R. Sadoway, M. K. Aydinol, Y. I. Jang, B. Huang, *Nature* **1998**, *392*, 694–696.
[57] J. Hong, W. E. Gent, P. Xiao, K. Lim, D.-H. Seo, J. Wu, P. M. Csernica, C. J. Takacs, D. Nordlund, C.-J. Sun, K. H. Stone, D. Passarello, W. Yang, D. Prendergast, G. Ceder, M. F. Toney, W. C. Chueh, *Nat. Mater.* **2019**, *18*, 256–265.
[58] C. Sun, X. Liao, F. Xia, Y. Zhao, L. Zhang, S. Mu, S. Shi, Y. Li, H. Peng, G. Van Tendeloo, K. Zhao, J. Wu, *ACS Nano* **2020**, *14*, 6181–6190.

Manuscript received: February 06, 2025
Revised manuscript received: March 24, 2025
Accepted manuscript online: March 27, 2025
Version of record online: ■■, ■■


© 2025 Wiley-VCH GmbH

15213757, 0, Downloaded from https://onlinelibrary.wiley.com/doi/10.1002/ange.202503100 by University Town Of Shenzhen, Wiley Online Library on [06/04/2025]. See the Terms and Conditions (https://onlinelibrary.wiley.com/terms-and-conditions) on Wiley Online Library for rules of use; OA articles are governed by the applicable Creative Commons License

# Forschungsartikel

**Batteries**

W. Zhao, M. Li, Z. Li, H. Ren, X. Wang, X. Yin, W. Ding, G. Chen, S. Chen, H. Yi*, S. Li, J. Wang, D. Zhou, L. Zhou, H. Lin, B. Fei, F. Pan*, Q. Zhao* — **e202503100**

Stabilizing Surface Lattice $O^{n-}$ $(0 < n < 2)$ for Long-Term Durability of $LiCoO_2$

This work constructs spinel and RS phases on the surface of LCO cathodes (named S-LCO and R-LCO). The spinel phase of S-LCO degrades during long-term cycling due to lattice $O^{n-}$ $(0 < n < 2)$ loss, while the RS phase of R-LCO remains stable due to its higher lattice $O^{n-}$ migration barriers. This study clarifies the mechanism of enhancing lattice $O^{n-}$ stability via phase tailoring, providing a basis for designing advanced LCO cathodes.

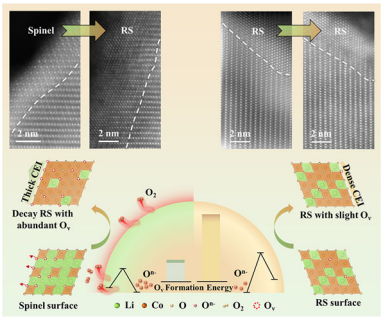




© 2025 Wiley-VCH GmbH

15213757, 0, Downloaded from https://onlinelibrary.wiley.com/doi/10.1002/ange.202503100 by University Town Of Shenzhen, Wiley Online Library on [06/04/2025]. See the Terms and Conditions (https://onlinelibrary.wiley.com/terms-and-conditions) on Wiley Online Library for rules of use; OA articles are governed by the applicable Creative Commons License